

# Holographic generative flows with AdS/CFT

Ehsan Mirafzali,<sup>1,\*</sup> Sanjit Shashi,<sup>1,2,†</sup> Sanya Murdeshwar,<sup>1</sup>  
Edgar Shaghoulian,<sup>2</sup> Daniele Venturi,<sup>3</sup> and Razvan Marinescu<sup>1</sup>

<sup>1</sup>*Department of Computer Science and Engineering,  
University of California, Santa Cruz, California, USA*

<sup>2</sup>*Santa Cruz Institute for Particle Physics, Department of Physics,  
University of California, Santa Cruz, California, USA*

<sup>3</sup>*Department of Applied Mathematics, University of California, Santa Cruz, California, USA*

We present a framework for generative machine learning that leverages the holographic principle of quantum gravity, or to be more precise its manifestation as the anti-de Sitter/conformal field theory (AdS/CFT) correspondence, with techniques for deep learning and transport theory. Our proposal is to represent the flow of data from a base distribution to some learned distribution using the bulk-to-boundary mapping of scalar fields in AdS. In the language of machine learning, we are representing and augmenting the flow-matching algorithm with AdS physics. Using a checkerboard toy dataset and MNIST, we find that our model achieves faster and higher quality convergence than comparable physics-free flow-matching models. Our method provides a physically interpretable version of flow matching. More broadly, it establishes the utility of AdS physics and geometry in the development of novel paradigms in generative modeling.

## I. INTRODUCTION

The field of generative machine learning has seen significant development in the past few years. While stochastic models like diffusion [1, 2] are still prominent, deterministic flow-based models have also been the subject of study and utilization. Such models were popularized through the framework of continuous normalizing flows (CNFs) [3, 4], which implement a log-likelihood loss and obey the dynamics of an ordinary differential equation rather than a stochastic one. However, training a CNF is slow and costly due to requiring simulation of the path obeying the ODE. Flow matching [5] addresses this issue by providing a simulation-free objective for learning the flow, leading to significant decreases to computational cost and increases in training efficiency.

While these models are entirely data-driven, they are often unable to exploit invariants or symmetries inherent in the data. Leveraging physical laws is one way to add additional inductive bias and structure into generative models [6, 7]. From a physicist’s perspective, mapping the flow to a process corresponding to some dynamical equation of motion seems natural, since the flow is dictated by its velocity (dynamics) and data (boundary conditions). Indeed, leveraging this idea to design a broader class of generative models was the motivation behind the GenPhys paradigm of [8]. Another approach is to embed the flow in an “extra” dimension, situating generation of  $d$ -dimensional datasets within the framework of  $(d+1)$ -dimensional differential geometry. This could facilitate the adaptation of formal mathematical tools to non-Euclidean machine learning (cf. [9]).

Together, these ideas are reminiscent of the holographic principle of quantum gravity [10, 11], in which



FIG. 1: The Poincaré disk as depicted by M.C. Escher’s Circle Limit IV print. The red circles represent constant radial slices. The angels and demons appear to shrink in size as we approach the edge of the disk, but in the hyperbolic metric their proper sizes remain constant.

a  $(d+1)$ -dimensional theory of gravity is dual to a non-gravitational field theory on a  $d$ -dimensional boundary. In other words, the gravitating geometry “emerges” from the field theory on the boundary, like a hologram. The most mathematically precise example of “holography” is the anti-de Sitter/conformal field theory (AdS/CFT) correspondence [12, 13]. AdS is a type of negatively curved or “hyperbolic” space like the Poincaré disk (Figure 1). Meanwhile, a CFT is a type of field theory that is symmetric with respect to scale transformations. In AdS/CFT, the CFT is supported on the boundary, and the “bulk” AdS physics defines a flow of  $d$ -dimensional physical theories along the radial direction [14, 15].

From the machine learning perspective, the CFT is analogous to the distribution describing some ground-truth data, and the radial direction is akin to a flow parameter. This is similar to analogies between AdS/CFT (and more broadly holography) and quantum error correction [16–18] and has been used to reinterpret AdS physics as a deep-learning network [19]—an approach leveraging machine learning for physics. However, that

\* [smirafza@ucsc.edu](mailto:smirafza@ucsc.edu)

† [sashashi@ucsc.edu](mailto:sashashi@ucsc.edu)

These authors contributed equally to this work.

work does not use the structure of AdS/CFT for typical machine learning tasks, such as data generation.

In this work, we build a flow-matching generative model that uses AdS/CFT physics as the fundamental engine guiding data generation (cf. [20]). Specifically, we choose a particular physical theory in AdS (Klein–Gordon scalar field theory) and use the boundary sources in the CFT as a proxy for the ground-truth data. We then perform an augmented, physics-informed version of flow matching, where the flow is designed to follow Klein–Gordon dynamics plus a residual correction learned by a neural network. This approach gives us the flexibility needed to generate various datasets that are not purely rooted in physical processes while still leveraging the analytic formulas of AdS physics.

To transmute raw data into physical quantities, we develop a “holographic encoding” method whereby training samples are treated as sources in the boundary CFT and projected into the bulk by some propagator. In testing our model, we find the following:

- Our method exhibits much more efficient convergence in terms of both the number of epochs and time than vanilla flow matching;
- Model performance improves as we decrease scalar mass within valid physical ranges; and,
- Flow-based models can also be designed on non-AdS spaces, but AdS is better.

We term our framework **Generative AdS** (GenAdS). Our results demonstrate that GenAdS has the potential to significantly aid data generation in machine learning.<sup>2</sup>

## Outline

We first discuss the necessary textbook physics in Section II, in which we introduce and explore the formulas of AdS–Klein–Gordon theory. Then in Section III, we review flow matching and discuss various modifications to the vanilla algorithm, particularly to the path and the losses, that allow for various facets in the model. We then elaborate on how we adapt holography and field theory to the flow matching paradigm in Section IV using our holographic encoding in conjunction with spectral techniques. In Sections V and VI, which respectively concern the checkerboard and MNIST datasets, we present our experiments and numerical results.

## II. KLEIN–GORDON THEORY IN AdS/CFT

We consider Klein–Gordon theory in AdS/CFT with two simplifying assumptions. First, we suppress gravitational backreaction, so we are only examining Klein–Gordon theory on a fixed AdS background. Second, we

restrict to maximally symmetric boundaries, so the bulk geometry is always described by a warped metric:

$$ds^2 = dr^2 + f(r)^2 \hat{g}_{ab} dx^a dx^b. \quad (1)$$

Here,  $ds^2$  is the line element,  $r$  is the radial direction,  $f$  is the warp factor, and  $\hat{g}_{ab}$  is the  $d$ -dimensional metric of the boundary whose indices  $a, b$  run from 1 to  $d$ , and the  $r$  dependence of the transverse slices is fully captured by the function  $f$ —meaning that  $\partial_r \hat{g}_{ab} = 0$ . The functional form of  $f$  depends on whether  $\hat{g}_{ab}$  is flat, spherical, or hyperbolic, which respectively correspond to  $f(r) = e^r$ ,  $\sinh r$ , and  $\cosh r$ . Furthermore, we work in Euclidean signature (so  $\hat{g}_{ab}$  is positive definite), rather than Lorentzian signature.

For a generic positive-definite metric  $g$ , the Klein–Gordon equations for a scalar field  $\Phi$  are

$$(\Delta_g - m^2) \Phi = 0, \quad \Delta_g \equiv \frac{1}{\sqrt{g}} \partial_\mu (\sqrt{g} g^{\mu\nu} \partial_\nu). \quad (2)$$

$\Delta_g$  is the Laplace–Beltrami (or Laplacian) operator on the metric  $g_{\mu\nu}$ . For the warped ansatz (1), this operator decomposes into partial derivatives of  $r$  and the Laplace–Beltrami operator  $\hat{\Delta}_g$  on  $\hat{g}_{ab}$ , which transmutes the Klein–Gordon equation into the following form:

$$\left[ \partial_r^2 + \frac{df'(r)}{f(r)} \partial_r + \frac{1}{f(r)^2} \hat{\Delta}_g - m^2 \right] \Phi = 0. \quad (3)$$

We now recast  $m^2$  in terms of a more convenient parameter  $\Delta$ . One of the core concepts in AdS/CFT is the “holographic dictionary,” which relates physical quantities in the bulk theory to those in the boundary theory. Scalar fields in AdS, for example, are dual to scalar operators in the CFT. In fact, there is a precise relationship between the squared-mass of  $\Phi$  and the scaling dimension (or energy)  $\Delta$  of the dual operator [21]:

$$m^2 = \Delta(\Delta - d). \quad (4)$$

We restrict ourselves to  $\Delta > d/2$  (a choice called “standard quantization”), so that there is no ambiguity in how the near-boundary modes of the scalar are associated with boundary data (cf. [22]). This does not exclude negative  $m^2$ , but such scalars are stable if they satisfy the Breitenlohner–Freedman bound  $m^2 > -d^2/4$  [23].

Before we proceed, we note that we do not work with the spherical or hyperbolic slicings of AdS in this paper. The details of solving Klein–Gordon depend upon the choice of topology, and the planar case is both the most tractable and sufficient as a first-pass demonstration of GenAdS. We leave the other cases to future work.

### II.1. Solving Klein–Gordon with propagators

To train our model, we need to map the ground-truth data to the bulk Klein–Gordon scalars. We discuss the details of our mapping later. Here, we address how one generally maps CFT quantities to AdS fields.

<sup>2</sup> The code is available at our [GitHub repository](#).

The inverse problem—extracting CFT information from AdS fields—is often accomplished with the use of the extrapolate dictionary [24, 25]. The key statement is that, in terms of the ansatz (1) and in standard quantization ( $\Delta > d/2$ ), Klein–Gordon scalars exhibit the following asymptotic behavior near the boundary:

$$\Phi(r, \vec{x}) \sim e^{-(d-\Delta)r} J(\vec{x}) + e^{-\Delta r} \frac{\langle O(\vec{x}) \rangle}{2\Delta - d}. \quad (5)$$

Here,  $\vec{x}$  represents the transverse coordinates,  $J$  is a source defined in the CFT, and  $\langle O \rangle$  is the vacuum expectation value (VEV) for the scalar operator  $O$ .

(5) is only an asymptotic solution, but we can treat it as a boundary condition. Then, formally, we can solve the Klein–Gordon equation in terms of the bulk-to-boundary propagator, which is a Green’s function with one of the insertion points taken to the boundary. We write this propagator as  $K(r, \vec{x}; \vec{x}')$ , where  $(r, \vec{x})$  is the bulk insertion point and  $\vec{x}'$  is the boundary insertion point.  $K$  has two defining properties; it must solve Klein–Gordon and exhibit  $\delta$ -function behavior in a particular boundary limit (given standard quantization):

$$\begin{aligned} (\Delta_g - m^2) K(r, \vec{x}; \vec{x}') &= 0, \\ \lim_{r \rightarrow \infty} e^{(d-\Delta)r} K(r, \vec{x}; \vec{x}') &\propto \delta(\vec{x} - \vec{x}'). \end{aligned} \quad (6)$$

These properties ensure that the convolution of the propagator with a source  $J$  solves the scalar field equation with asymptotic behavior (5) up to an overall factor, so we make the identification

$$\Phi(r, \vec{x}) \equiv \int d^d x' \sqrt{\hat{g}} K(r, \vec{x}; \vec{x}') J(\vec{x}'). \quad (7)$$

We can write  $K$  explicitly. First, define

$$C_\Delta \equiv \frac{\Gamma(\Delta)}{\pi^{d/2} \Gamma(\Delta - d/2)}. \quad (8)$$

This is the normalization factor that ensures agreement between (7) and (5). The planar propagator is

$$K(r, \vec{x}; \vec{x}') = \frac{C_\Delta}{(e^r |\vec{x} - \vec{x}'|^2 + e^{-r})^\Delta}, \quad (9)$$

where  $|\vec{x} - \vec{x}'|$  is the Euclidean distance between the points  $\vec{x}$  and  $\vec{x}'$ . If we parameterize the transverse directions in terms of Cartesian coordinates  $(x_1, \dots, x_d)$ , then we can write  $|\vec{x} - \vec{x}'| = \sqrt{(x_1 - x'_1)^2 + \dots + (x_d - x'_d)^2}$ .

## II.2. Spectral decomposition of Klein–Gordon

The standard flow-matching procedure [5] is dictated by a first-order differential ODE [3]. In contrast, the Klein–Gordon equation (3) is a PDE. In this subsection, we recast the PDE as a set of ODEs.

To do so, we can perform a spectral decomposition of the transverse Laplacian  $\hat{\Delta}_g$ . Generically, the starting point is to find the eigenfunctions  $Y_\lambda^\alpha(\vec{x})$  satisfying

$$\hat{\Delta}_g Y_\lambda^\alpha(\vec{x}) = -\lambda Y_\lambda^\alpha(\vec{x}). \quad (10)$$

$\lambda$  labels the spectral modes and is discrete for bounded spaces and continuous otherwise.  $\alpha$  is the degeneracy label at a given  $\lambda$ . We impose orthonormality (with bars for complex conjugation),

$$\int d^d x \sqrt{\hat{g}} \sum_\alpha Y_\lambda^\alpha(\vec{x}) \bar{Y}_{\lambda'}^\alpha(\vec{x}) = \delta(\lambda - \lambda') \delta_{\alpha\alpha'}. \quad (11)$$

$\delta(\lambda - \bar{\lambda})$  is a  $\delta$  function with respect to some generic integration measure  $d\mu_\lambda$ . Mathematically, this means that  $\int d\mu_\lambda f(\lambda) \delta(\lambda - \lambda') = f(\lambda')$  for any function  $f$ . Furthermore, (11) implies a completeness relation:

$$\delta(\vec{x} - \vec{x}') = \int d\mu_\lambda \sum_\alpha Y_\lambda^\alpha(\vec{x}) \bar{Y}_\lambda^\alpha(\vec{x}'). \quad (12)$$

Let us now apply this machinery to Klein–Gordon theory. Since we are only considering maximally symmetric transverse slices, we can write the spectral expansion for the scalar field as

$$\Phi(r, \vec{x}) = \int d\mu_\lambda \phi_\lambda(r) \sum_\alpha Y_\lambda^\alpha(\vec{x}), \quad (13)$$

where the mode coefficients  $\phi_\lambda(r)$  do not depend on the degeneracy label. From the second-order Klein–Gordon equation, we get the following ODE:

$$\frac{d^2 \phi_\lambda}{dr^2} + \frac{df'(r)}{f(r)} \frac{d\phi_\lambda}{dr} = \left[ \frac{\lambda}{f(r)^2} + \Delta(\Delta - d) \right] \phi_\lambda(r). \quad (14)$$

We can also write an expansion for the bulk-to-boundary propagator. Since it depends on  $\vec{x}$  and  $\vec{x}'$ , it takes the form

$$K(r, \vec{x}; \vec{x}') = \int d\mu_\lambda \kappa_\lambda(r) \sum_\alpha Y_\lambda^\alpha(\vec{x}) \bar{Y}_\lambda^\alpha(\vec{x}'). \quad (15)$$

The mode coefficients  $\kappa_\lambda$  also satisfy (14). They are related to the  $\phi_\lambda$  coefficients through the coefficients of the source  $J$ :

$$\phi_\lambda(r) = j_\lambda \kappa_\lambda(r), \quad J(\vec{x}) = \int d\mu_\lambda j_\lambda \sum_\alpha Y_\lambda^\alpha(\vec{x}). \quad (16)$$

Let us now write out the spectral eigenbasis for flat space, which is unbounded and thus furnishes a continuous spectrum. A calculation shows that plane waves with momentum  $\vec{k} = (k_1, \dots, k_d)$  are eigenfunctions of the Laplacian:

$$\hat{\Delta}_g e^{-i\vec{k} \cdot \vec{x}} = -|\vec{k}|^2 e^{-i\vec{k} \cdot \vec{x}}. \quad (17)$$

So the spectral basis is simply a Fourier basis  $\{e^{-i\vec{k} \cdot \vec{x}}\}$ , with the spectral label being the (Euclidean) norm of the momentum. As such, the integration measure over the modes (including degeneracies) is the flat one on momentum space  $d^d k$ . To normalize, we note that

$$\int d^d k e^{-i\vec{k} \cdot \vec{x}} e^{i\vec{k} \cdot \vec{x}'} = (2\pi)^d \delta(\vec{x} - \vec{x}'). \quad (18)$$

So, we take the basis

$$Y_{\vec{k}}(\vec{x}) \equiv \frac{1}{(2\pi)^{d/2}} e^{-i\vec{k}\cdot\vec{x}}. \quad (19)$$

We can now compute the coefficients of the propagator by performing a Fourier transform of (9),

$$\begin{aligned} \kappa_{|\vec{k}|}(r) &= \int d^d x e^{i\vec{k}\cdot\vec{x}} K(r, \vec{x}; 0) \\ &= \frac{2}{\Gamma(\nu)} e^{-dr/2} \left( \frac{|\vec{k}|}{2} \right)^\nu K_\nu(|\vec{k}| e^{-r}). \end{aligned} \quad (20)$$

$K_\nu$  is the modified Bessel function of the second kind, and out of convenience we have defined  $\nu \equiv \Delta - d/2$ .

### II.3. First-order formulation

To use Klein–Gordon dynamics in flow matching, we still need to rewrite it in its first-order formulation. We do so by first defining the canonical momentum field,

$$\Pi \equiv \partial_r \Phi. \quad (21)$$

Then, we can rewrite the Klein–Gordon equation in terms of Hamilton’s equations, which are a set of first-order equations:

$$\partial_r \Phi = \Pi, \quad (22)$$

$$\partial_r \Pi = \left[ \Delta(\Delta - d) - \frac{1}{f(r)^2} \hat{\Delta}_g \right] \Phi - \frac{df'(r)}{f(r)} \Pi. \quad (23)$$

We can also write (22)–(23) as ODEs of the spectral mode coefficients  $\phi_\lambda$  and  $\pi_\lambda$ ,

$$\frac{d\phi_\lambda}{dr} = \pi_\lambda(r), \quad (24)$$

$$\frac{d\pi_\lambda}{dr} = \left[ \frac{\lambda}{f(r)^2} + \Delta(\Delta - d) \right] \phi_\lambda(r) - \frac{df'(r)}{f(r)} \pi_\lambda(r). \quad (25)$$

(24)–(25) define a trajectory in phase space and provide inductive bias in our model, as we see in Section III.

### II.4. Numerical stabilization of fields

The asymptotic behavior of  $\Phi$  in (5) immediately indicates a numerical issue. The term containing the source rapidly decays to 0 near the boundary, but in our model we need to extract it. We find it helpful to perform the following field redefinition:

$$\tilde{\Phi} \equiv e^{(d-\Delta)r} \Phi, \quad \tilde{\Pi} \equiv e^{(d-\Delta)r} [\Pi + (d - \Delta)\Phi]. \quad (26)$$

This makes the VEV term in (5) decay exponentially for all  $\Delta > d/2$ , whereas the source term is  $O(1)$ , so we can properly isolate the latter from the former numerically.

Furthermore, the redefined fields satisfy a slightly different version of the first-order Klein–Gordon equations,

which in planar AdS and in terms of the spectral mode coefficients  $\tilde{\phi}_{\vec{k}}$  and  $\tilde{\pi}_{\vec{k}}$  are

$$\frac{d\tilde{\phi}_{\vec{k}}}{dr} = \tilde{\pi}_{\vec{k}}(r), \quad (27)$$

$$\frac{d\tilde{\pi}_{\vec{k}}}{dr} = |\vec{k}|^2 e^{-2r} \tilde{\phi}_{\vec{k}}(r) - (2\Delta - d) \tilde{\pi}_{\vec{k}}(r). \quad (28)$$

We should also mention the changes to the propagator. Based on (7), the redefined propagator is simply

$$\tilde{K} \equiv e^{(d-\Delta)r} K. \quad (29)$$

In the spectral decomposition, this only modifies the mode coefficients by a factor of  $e^{(d-\Delta)r}$ , so they are now

$$\tilde{\kappa}_{|\vec{k}|}(r) = \frac{2}{\Gamma(\nu)} \left( \frac{|\vec{k}| e^{-r}}{2} \right)^\nu K_\nu(|\vec{k}| e^{-r}). \quad (30)$$

## III. ELEMENTS OF FLOW MATCHING

We have discussed the necessary physics, so let us now elaborate on the necessary ML theory. We review the mathematics underlying the flow-matching approach of [5] and discuss the modifications made in our model.

First, however, we establish conventions. Throughout this section, we use the shorthand  $S \equiv (\tilde{\Phi}, \tilde{\Pi})$  to represent a point in (redefined) phase space (26). The  $\tilde{\Phi}$  and  $\tilde{\Pi}$  components of a function in this phase space are written with superscripts, i.e.  $\Psi = (\Psi^{\tilde{\Phi}}, \Psi^{\tilde{\Pi}})$ . Furthermore, we condense the first-order Klein–Gordon equations as  $\partial_r S = V_{\text{KG}}$ , where

$$V_{\text{KG}} = \left( \tilde{\Pi}, -e^{-2r} \hat{\Delta}_g \tilde{\Phi} - (2\Delta - d) \tilde{\Pi} \right). \quad (31)$$

The flows are paths in phase space parameterized by the radial direction of AdS. As a regularization procedure, we truncate the flows at  $r = r_{\text{IR}}$  and  $r = r_{\text{UV}}$ , which respectively correspond to the deep-bulk and near-boundary regions. Furthermore, we use a compact “time” coordinate  $t \in [0, 1]$ , which is related to  $r$  as

$$r(t) = (r_{\text{UV}} - r_{\text{IR}})t + r_{\text{IR}}. \quad (32)$$

We then write the flows as  $S_t$ . Each point  $S_0$  samples a base distribution (such as a Gaussian), whereas each point  $S_1$  samples the target distribution of interest.

The idea in flow matching is to train a network to learn a velocity field  $V_t$ . Once we do so, we can sample the base distribution and use numerical integration to generate from the target.

### III.1. Flows and log-likelihood computation

We first review the mathematical foundations of flow-based generation. The dynamics of any flow-based model are defined by an ODE of the form

$$\frac{dS_t}{dt} = V_t(\theta), \quad (33)$$

where the velocity  $V_t(\theta)$  is a neural network parameterized by  $\theta$ . This is called a “neural” ODE [3]. The idea of the continuous-normalizing-flow (CNF) method is to transport a probability density along this velocity field. As probability mass is conserved at each time slice, we can write a continuity equation

$$\frac{\partial p_t}{\partial t} = -\nabla_a (p_t V_t^a), \quad (34)$$

where  $a$  is an index over the dimensions of the space hosting the flows and  $p_t$  is the probability density at time  $t$ . In our case, the flows live in an intrinsically flat phase space, so we can integrate to write the log likelihood:

$$\log p_1 = \log p_0 - \int_0^1 dt \left( \frac{\partial V_t^{\tilde{\Phi}}}{\partial \tilde{\Phi}} + \frac{\partial V_t^{\tilde{\Pi}}}{\partial \tilde{\Pi}} \right). \quad (35)$$

In CNF [3, 4], we implement a log-likelihood loss, but this is computationally intensive because evaluating the log likelihood involves numerical integration.

### III.2. Linear versus Hermite paths

The main upshot of flow matching versus other generative methods (particularly CNF) is the relatively inexpensive training. This is because we assume a particular path for the transport of data from the base distribution to the target distribution, so training is integration-free.

In vanilla flow matching [5], this path is linear. In terms of the time parameter  $t$ , the path is

$$S_t = (1-t)S_0 + tS_1, \quad (36)$$

where  $S_0$  and  $S_1$  are the initial and final points, respectively.  $S_0$  is sampled from some base distribution such as a Gaussian, whereas  $S_1$  is sampled from the ground-truth distribution. The velocity is then  $\partial_t S_t = S_1 - S_0$ , and we train a neural network to learn this quantity.

Linear paths are computationally simple. However, they are also off-shell, in that they do not restrict to the Lagrangian submanifold of phase space, i.e. they do not respect the first Klein–Gordon equation  $\partial_r \tilde{\Phi} = \tilde{\Pi}$ . To see this, we can differentiate the  $\tilde{\Phi}$  component with respect to the radial direction  $r$  and impose the constraints  $\tilde{\Pi}_0 = \partial_r \tilde{\Phi}_0$  and  $\tilde{\Pi}_1 = \partial_r \tilde{\Phi}_1$  to write

$$\partial_r \tilde{\Phi}_t = \tilde{\Pi}_t + (r_{\text{UV}} - r_{\text{IR}})(\tilde{\Phi}_1 - \tilde{\Phi}_0). \quad (37)$$

For the path to stay on-shell, we should have  $\partial_r \tilde{\Phi}_t = \tilde{\Pi}_t$ .

This motivates an alternate construction of the phase-space path. We write an interpolation ansatz for just  $\tilde{\Phi}_t$ , then define  $\tilde{\Pi}_t$  as  $\partial_r \tilde{\Phi}_t$ . We also have four constraints at the endpoints—two for  $\tilde{\Phi}$  and two for  $\tilde{\Pi}$ . The minimal choice is thus to write  $\tilde{\Phi}_t$  as a cubic curve, which we write in terms of the cubic Hermite basis:

$$\begin{aligned} H_{00}(u) &= 2u^3 - 2u^2 + 1, & H_{01}(u) &= -2u^3 + 3u^2, \\ H_{10}(u) &= u^3 - 2u^2 + u, & H_{11}(u) &= u^3 - u^2. \end{aligned} \quad (38)$$

For this interpolation to work properly, we find it useful to use another path parameter  $u \in [0, 1]$  that accounts for the changing volumes of the radial slices of AdS as  $r$  runs from  $r_{\text{IR}}$  to  $r_{\text{UV}}$ . We define

$$u(r) = \left[ \int_{r_{\text{IR}}}^{r_{\text{UV}}} \frac{dr'}{\sqrt{g(r')}} \right]^{-1} \int_{r_{\text{IR}}}^r \frac{dr'}{\sqrt{g(r')}}, \quad (39)$$

which for planar AdS is computed to be

$$u(r) = \frac{1 - e^{-d(r-r_{\text{IR}})}}{1 - e^{-d(r_{\text{UV}}-r_{\text{IR}})}}. \quad (40)$$

We then write the path as

$$\begin{aligned} \tilde{\Phi}_u &= H_{00}(u)\tilde{\Phi}_0 + H_{01}(u)\tilde{\Phi}_1 \\ &\quad + H_{10}(u)m_0 + H_{11}(u)m_1, \end{aligned} \quad (41)$$

where

$$m_0 = \left( \frac{dr}{du} \right) \Big|_{r_{\text{IR}}} \tilde{\Pi}_0, \quad m_1 = \left( \frac{dr}{du} \right) \Big|_{r_{\text{UV}}} \tilde{\Pi}_1. \quad (42)$$

Then,  $\tilde{\Phi}_t$  is written by substituting  $u \rightarrow r \rightarrow t$ , and  $\tilde{\Pi}_t$  is obtained by computing  $\partial_r \tilde{\Phi}_t$ .

### III.3. Losses and residuals

Now that we have both the linear and Hermite paths, we can write the losses associated with both. Prior to doing so, however, it is helpful to define

$$\delta_r \equiv \frac{dr}{dt} = r_{\text{UV}} - r_{\text{IR}}, \quad (43)$$

since the velocities used in the losses are derivatives with respect to the  $t$  parameter written in (32).

The  $\tilde{\Phi}$  and  $\tilde{\Pi}$  velocities for the linear path are

$$U_t^{\tilde{\Phi}} = \delta_r(\tilde{\Phi}_1 - \tilde{\Phi}_0), \quad U_t^{\tilde{\Pi}} = \delta_r(\tilde{\Pi}_1 - \tilde{\Pi}_0). \quad (44)$$

As for the Hermite path, the velocities are

$$\begin{aligned} U_t^{\tilde{\Phi}} &= \delta_r \tilde{\Pi}_t, \\ U_t^{\tilde{\Pi}} &= \delta_r \left[ \left( \frac{du}{dr} \right)^2 \partial_u^2 \tilde{\Phi}_t + \frac{d^2 u}{dr^2} \partial_u \tilde{\Phi}_t \right]. \end{aligned} \quad (45)$$

The idea is to train a time-dependent neural network  $V_t(\theta)$  with parameters  $\theta$  to learn these velocities. This might be done with a time-averaged mean squared error loss. However, we want the loss to respect the warped metric structure (1), so we define

$$\mathcal{L} = \left\langle \left| \left| V_t(\theta) - U_t \right| \right|_{g_r(t)}^2 \right\rangle_t. \quad (46)$$

The averaging  $\langle \cdot \rangle$  is also implicitly over the initial and final samples, and for a generic function  $\Psi(S)$  in phase space, the norm  $\|\cdot\|_{g_r}$  is defined as

$$\begin{aligned} \left\| \Psi(S) \right\|_{g_r(t)}^2 &= \int d^d x f(r)^d |\Psi^{\tilde{\Phi}}(r, \vec{x})|^2 \\ &\quad + \int d^d x f(r)^d |\Psi^{\tilde{\Pi}}(r, \vec{x})|^2. \end{aligned} \quad (47)$$

This is a sum weighted by the transverse slices' volumes.

We have not yet included Klein–Gordon. To do so, we can consider another network  $R_t(\theta)$  and substitute

$$V_t(\theta) \rightarrow \delta_r V_{\text{KG}} + R_t(\theta). \quad (48)$$

The Klein–Gordon equation thus acts as a backbone velocity, and  $R_t(\theta)$  is the residual learned by the neural network. The loss is then

$$\mathcal{L} = \left\langle \|R_t(\theta) - (U_t - \delta_r V_{\text{KG}})\|_{g_{r(t)}}^2 \right\rangle_t. \quad (49)$$

At this point, we can make two choices—whether or not we want to include the Klein–Gordon backbone and the type of path we use. If we have a Klein–Gordon term in the loss, then both paths are available to us. However, note that the Hermite path by construction already satisfies the first Klein–Gordon equation, so training would drive  $R_t^{\tilde{\Phi}}$  to 0. Thus for the Hermite path, we can just set  $R_t^{\tilde{\Phi}}(\theta) = 0$  and train only the  $\tilde{\Pi}$  component.

#### IV. DESIGNING THE MODEL

We now elaborate on how we integrate flow matching into a physical framework. The idea is to use holography to translate the raw data (such as an image) into physical fields. To this end, we define a “holographic encoding” procedure. We then use the phase-space flow-matching machinery discussed in Section III in Fourier space, with a convolutional architecture chosen for the network so as to impose the appropriate inductive bias.

##### IV.1. Holographic encoding

To translate raw data into physical data, we define a “holographic encoding” algorithm. Generically, we identify a given sample drawn from the ground-truth distribution with a boundary source  $J_*(\vec{x})$ , which we then convolve with the bulk-to-boundary propagator as in (7). This gives the encoding of the sample as a scalar field:

$$\Phi(r, \vec{x}|J_*) = \int d^d \vec{x}' K(r, \vec{x}; \vec{x}') J_*(\vec{x}'). \quad (50)$$

We then use  $\Phi(r_{\text{UV}}, \vec{x}|J_*)$  as training data.

For example, for 2-dimensional data, we use the following “point” encoding. Taking the number of boundary dimensions to be  $d = 2$ , each sample is simply a point  $\vec{x}_* \in \mathbb{R}^2$  that we map to a  $\delta$  source in the boundary CFT:

$$J_*(\vec{x}) = \delta(\vec{x} - \vec{x}_*). \quad (51)$$

Using (50), the field at the boundary is

$$\Phi(r_{\text{UV}}, \vec{x}|J_*) = K(r_{\text{UV}}, \vec{x}; \vec{x}_*). \quad (52)$$

For an image, we identify  $J_*$  with the pixel intensity map. The resulting integral in (50) cannot be evaluated outright, but we can instead compute the field in Fourier space by spectrally decomposing the source.

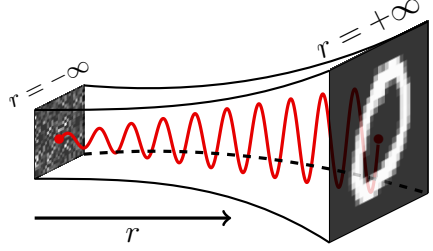


FIG. 2: A schematic representation of the holographic encoding for a sample of the MNIST dataset. The image is treated as a source on the boundary for the corresponding bulk field, which flows to noise.

To train the model, we have the neural network learn the velocity of a flow from a noise profile deep in the bulk to the holographic encoding near the boundary. This idea is schematically represented by Figure 2.

##### IV.2. Spectral representation of data

We reiterate that flow matching needs ODEs, not PDEs, so we need to transmute all of the above technology into Fourier space. Doing so is also necessary for holographic encoding of images, since working in Fourier space allows us to compute (50).

Given a Fourier mode with momentum  $\vec{k}$ , we can compute the corresponding mode coefficient for the phase-space encoding of a sample algebraically using (16):

$$\begin{aligned} \phi_{\vec{k}}(r_{\text{UV}}|J_*) &= j_{*\vec{k}} \kappa_{|\vec{k}|}(r_{\text{UV}}), \\ \pi_{\vec{k}}(r_{\text{UV}}|J_*) &= j_{*\vec{k}} \partial_r \kappa_{|\vec{k}|}(r_{\text{UV}}). \end{aligned} \quad (53)$$

$j_{*\vec{k}}$  is the mode coefficient of the associated source,

$$j_{*\vec{k}} = \int \frac{d^d x}{(2\pi)^{d/2}} e^{i\vec{k} \cdot \vec{x}} J_*(\vec{x}). \quad (54)$$

For example, the mode coefficients of the  $\delta$  source (51) are  $e^{i\vec{k} \cdot \vec{x}_*}/(2\pi)^{d/2}$ , so we have the following fields in Fourier space

$$\begin{aligned} \phi_{\vec{k}}(r_{\text{UV}}|\vec{x}_*) &= \frac{1}{(2\pi)^{d/2}} \kappa_{|\vec{k}|}(r_{\text{UV}}) e^{i\vec{k} \cdot \vec{x}_*}, \\ \pi_{\vec{k}}(r_{\text{UV}}|\vec{x}_*) &= \frac{1}{(2\pi)^{d/2}} \partial_r \kappa_{|\vec{k}|}(r_{\text{UV}}) e^{i\vec{k} \cdot \vec{x}_*}, \end{aligned} \quad (55)$$

Thus in this “spectral” point encoding, the position of the sample  $\vec{x}_*$  is described by a phase factor  $e^{i\vec{k} \cdot \vec{x}_*}$ .

In our code, we make use of the analogous equations for the redefined fields discussed in Section II.4. Specifically, we use (30) to write

$$\tilde{\phi}_{\vec{k}}(r_{\text{UV}}|J_*) = \frac{2j_{*\vec{k}}}{\Gamma(\nu)} \left( \frac{|\vec{k}| e^{-r_{\text{UV}}}}{2} \right)^\nu K_\nu(|\vec{k}| e^{-r_{\text{UV}}}), \quad (56)$$

$$\tilde{\pi}_{\vec{k}}(r_{\text{UV}}|J_*) = \frac{4j_{*\vec{k}}}{\Gamma(\nu)} \left( \frac{|\vec{k}| e^{-r_{\text{UV}}}}{2} \right)^{\nu+1} K_{\nu-1}(|\vec{k}| e^{-r_{\text{UV}}}).$$

### IV.3. Convolutional networks for spectral flows

We now discuss how to implement a flow in Fourier space. The first step is to bound the transverse space, which induces a discretization of the Fourier space. Specifically if we truncate each component spatial component  $x_i$  to an interval of length  $L_i$ , then each momentum component  $k_i$  is quantized:

$$k_i = \frac{2\pi m}{L_i}, \quad m \in \mathbb{Z}. \quad (57)$$

For simplicity, we say that each interval has the same length. Furthermore, for regularization purposes, we take  $K$  modes for each component  $k_i$ . With these approximations made, the Fourier space becomes a finite  $d$ -dimensional grid with  $K^d$  points, with each point associated to a particular set of mode coefficients.

The goal is to train a network to learn the velocities (or residual velocities) of all of the chosen mode coefficients, that is  $d\tilde{\phi}_{\vec{k}}/dt$  and  $d\tilde{\pi}_{\vec{k}}/dt$ . As the inputs and outputs of the network are arranged on a grid, it is natural to use a convolutional neural network (CNN) so as to inject inductive bias towards translational equivariance.

How do we train such a network? We exploit the fact that integrals over Fourier space  $\int d^d k$  reduce to discrete, finite sums over the chosen momenta when we work on a finite grid. In particular, the norm  $\|\cdot\|_{g_{r(t)}}^2$  used in the loss (46) becomes easily computable. Writing the mode coefficients of  $\Psi = (\Psi^{\tilde{\Phi}}, \Psi^{\tilde{\Pi}})$  as  $\psi_{\vec{k}}^{\tilde{\Phi}}$  and  $\psi_{\vec{k}}^{\tilde{\Pi}}$ , we have that

$$\|\Psi(S)\|_{g_{r(t)}}^2 = \sum_{\vec{k}} f(r)^d \left( |\psi_{\vec{k}}^{\tilde{\Phi}}|^2 + |\psi_{\vec{k}}^{\tilde{\Pi}}|^2 \right). \quad (58)$$

As for the endpoints of the flow used in training, the samples at  $t = 1$  ( $r = r_{UV}$ ) are mathematically expressed as (56), whereas the base samples at  $t = 0$  ( $r = r_{IR}$ ) for each pair of Fourier mode coefficients  $\tilde{\phi}_{\vec{k}}$  and  $\tilde{\pi}_{\vec{k}}$  are drawn from Gaussians:

$$\begin{aligned} \tilde{\phi}_{\vec{k}}(r_{IR}) &\sim \mathcal{N}(0, c_\phi(1 + |\vec{k}|^2)^{-s_\phi}), \\ \tilde{\pi}_{\vec{k}}(r_{IR}) &\sim \mathcal{N}(0, c_\pi(1 + |\vec{k}|^2)^{-s_\pi}). \end{aligned} \quad (59)$$

After training, we numerically integrate the resulting learned velocity with samples of these distributions acting as initial values in order to generate new data. Specifically, this integration procedure gives us a set of  $K^d$  Fourier mode coefficients at the AdS boundary that we can then decode.

We note that the decoding procedure is different between images and points. For images, we simply use the mode coefficients for the scalar field to reconstruct the source in position space, which is then interpreted as an intensity map for the generated image. For points, however, the generated source is actually a collection of  $K^d$  points in data space, so we also average over these points' positions to extract a single point.

## V. CHECKERBOARD EXPERIMENTS

To test our model, we utilize toy point-cloud datasets with known ground-truth distribution. Specifically, we train our models on the checkerboard distribution, which was also used in the original flow-matching paper [5].

For all of the models shown here, most of the hyperparameters are kept fixed. The checkerboard is supported on two dimensions, so  $d = 2$ . The velocity CNN has 10,596,868 parameters when computing the Hermite path and 10,599,176 parameters for the linear path. We always train on 50,000 samples with batch size 64, and we use AdamW with learning rate  $3 \times 10^{-4}$  and weight decay  $1 \times 10^{-5}$ . Generated datasets have 10,000 points.

The flow-matching machinery has additional hyperparameters. The  $r$  cutoffs for the flow are taken to be  $r_{IR} = 0$  and  $r_{UV} = 1$ . For the spectral machinery, we truncate the transverse planar space to a square with width  $L = 8$  and take  $K = 16$ , so there are 256 Fourier modes included in our sums. Lastly, the parameters for the base distributions (59) are

$$c_\phi = 1.0, \quad c_\pi = 0.55, \quad s_\phi = 1.0, \quad s_\pi = 1.0. \quad (60)$$

For each experiment, we state the number of epochs and the value or values of  $\Delta$  explicitly.

As the checkerboard is a 2d distribution, we make use of the point encoding discussed in Section IV.1. The ground-truth samples are thus represented by the Fourier mode coefficients (56), with

$$j_{*\vec{k}} = \frac{e^{i\vec{k} \cdot \vec{x}_*}}{2\pi}. \quad (61)$$

### V.1. Checkerboard metrics

There are two potential points of failure in learning the checkerboard; a model might generate points in the blank regions and it might develop non-uniformities within the tiles. We define and compute metrics measuring both.

The former issue can be diagnosed with a “boundary violation” (BV) statistic. This is simply a count of the fraction of generated points  $y_j$  that fall outside valid checkerboard cells. BV quantifies the failure of the model to learn the location of the checkerboard’s boundaries.

For the latter, we use the “within-cell” energy distance (WED). For two distributions  $P$  and  $Q$  and sample points  $\vec{x}, \vec{x}' \sim P$  and  $\vec{y}, \vec{y}' \sim Q$ ,

$$ED = 2 \langle |\vec{x} - \vec{y}| \rangle_{P,Q} - \langle |\vec{x} - \vec{x}'| \rangle_P - \langle |\vec{y} - \vec{y}'| \rangle_Q. \quad (62)$$

where  $|\cdot|$  is Euclidean distance.

We compute WED by first evaluating the energy distance within each individual checkerboard tile between the model and ground-truth samples, then computing a sum of these weighted by the number of true points per cell. Since the checkerboard is uniform within each cell, WED measures local non-uniformity of the learned distribution.

	AdS + KG (H)	AdS + KG (L)	AdS	Baseline FCN
Model distributions				
BV	<b>0.0374 ± 0.0020</b>	0.0412 ± 0.0025	0.0433 ± 0.0014	0.0836 ± 0.0016
WED	0.0320 ± 0.0086	<b>0.0247 ± 0.0088</b>	0.0326 ± 0.0045	0.0353 ± 0.0068
$t_{\text{ep}}$	10.565 ± 0.104 s	10.187 ± 0.066 s	9.978 ± 0.078 s	6.282 ± 0.060 s
$t_{\text{inf}}$	111.692 ± 0.003 s	111.695 ± 0.006 s	110.779 ± 0.046 s	12.366 ± 0.039 s
$t_{\text{thr}}$	432.914 ± 19.820 s	344.866 ± 97.418 s	282.564 ± 4.378 s	536.180 ± 8.544 s

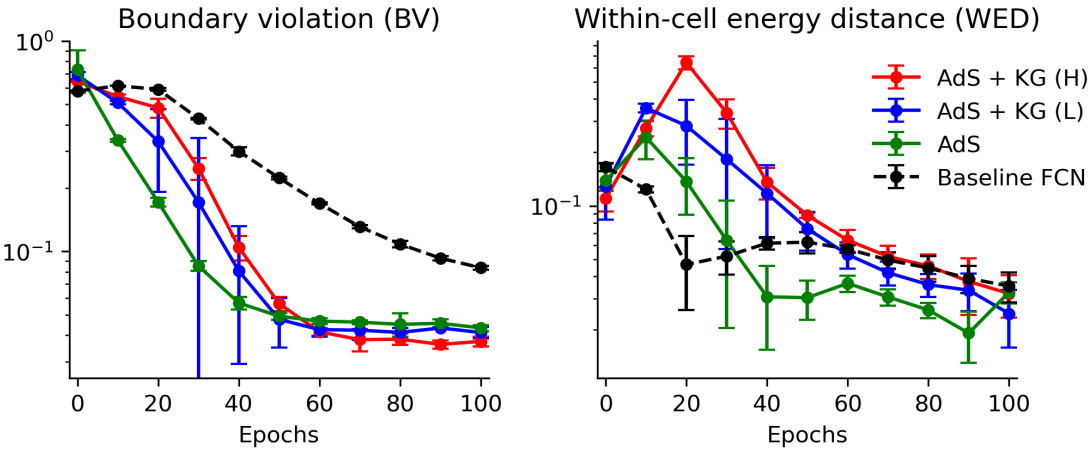


FIG. 3: We present the learned distributions of models trained on the checkerboard after 100 epochs. The **AdS + KG (H)** and **AdS + KG (L)** models are trained with the loss (49), using Hermite and linear paths respectively, and the **AdS** model is trained with the loss (46) and a linear path. The **Baseline FCN** uses no AdS information. We also show the final boundary-violation (BV) and within-cell-energy-distance (WED) metrics, the time per epoch  $t_{\text{ep}}$ , final inference time  $t_{\text{inf}}$  for 10,000 samples, and estimated threshold time  $t_{\text{thr}}$  when  $\text{BV} < 0.1$  (assuming linearity of BV within each 10-epoch interval), all averaged over three seeds. Additionally, we plot the BV and WED metrics.

## V.2. Ablations with checkerboards

In Figure 3, we show the results of an ablation study of four models. Our GenAdS models (with  $\Delta = 1.5$ ) are:

- (1) A Klein–Gordon residual model trained with the loss (49) and a Hermite path (45);

(2) A Klein–Gordon residual model trained with the loss (49) and with a linear path (44); and,

(3) A model with the loss (46) and a linear path (44).

We compare against an FCN with 10,601,588 parameters trained to perform flow matching without any AdS information. To make the comparison fair, we still map the raw data to the field  $\tilde{\Phi}$  (treating  $\tilde{\Pi}$  as ancillary).

All of the models are comparable according to WED. The main difference is shown by BV. The GenAdS models are consistently more efficient at learning the checkerboard boundaries than the FCN. Each GenAdS model, and notably not the FCN, exhibits a sharp early decrease in BV, which corresponds to the emergence of multimodality in the learned distribution.

There is a tradeoff, however; the GenAdS models take roughly twice as long to train. Nonetheless, the increase in per-epoch training time is offset by the higher per-epoch efficiency of GenAdS.

### V.3. Modulating scalar masses in AdS

The hyperparameter  $\Delta$  corresponds to the mass of the scalar field in AdS through the mass-dimension relation, which for  $d = 2$  is  $m^2 = \Delta(\Delta - 2)$ . It is natural to probe the effect of varying  $\Delta$ . We examine

$$\Delta = 1.5, 2, 2.5, 3 \implies m^2 = -0.75, 0, 1.25, 3. \quad (63)$$

In the models shown in Figure 4, performance degrades as  $\Delta$  increases. This is evident in the plots and the statistics; BV and WED are both much larger for the  $\Delta > 2$  models.  $\Delta = 1.5$  and  $2.0$  appear comparable, but the latter has a much lower WED.

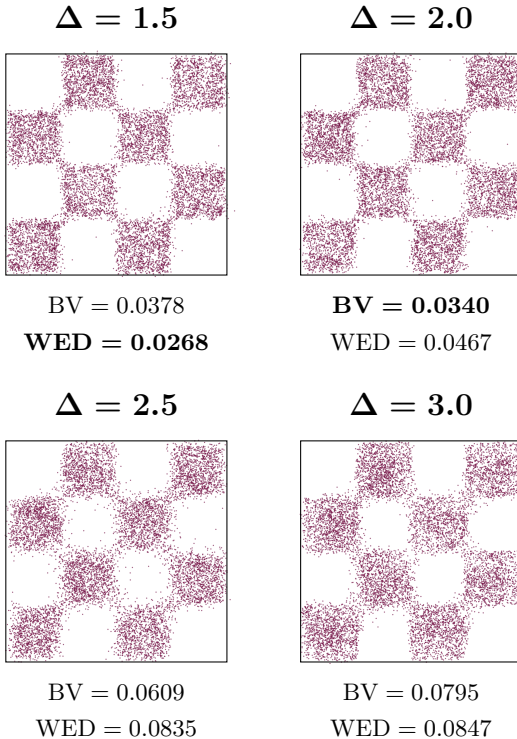


FIG. 4: The results from varying the scaling dimension  $\Delta$ , which corresponds to the bulk scalar's squared-mass  $m^2 = \Delta(\Delta - 2)$ . These models are trained to 100 epochs. The models degrade when  $\Delta \geq 2$ , suggesting the optimal choice might generally be  $\Delta < 2$ , which corresponds to a relevant scalar operator on the boundary.

### V.4. Interpolating between flat space and AdS

So far we have only invoked AdS/CFT, but our flow-matching machinery can be adapted to any geometry. So does the use of AdS in our model actually make an appreciable difference in performance? One way to probe this question is to consider the class of “hyperscaling-violating” (HSV) geometries [26] (see Appendix A):

$$ds^2 = dr^2 + \frac{1}{(pr)^{2\gamma}} d\vec{x}^2, \quad \gamma \equiv \frac{1}{p} - 1, \quad (64)$$

where  $p \in (0, 1]$  is the interpolation parameter and the boundary is at  $r = 0$ . Taking  $p \rightarrow 1$  ( $\gamma = 0$ ) yields flat space, and  $p \rightarrow 0$  ( $\gamma \rightarrow \infty$ ) is the AdS limit.

As in GenAdS, we represent the data with scalar fields. However, HSV is more limited. The solution to Klein-Gordon (3) is only analytically tractable for  $m^2 = 0$ . The details and formulas are discussed in Appendix A.

We train massless HSV models with interpolation parameter  $p \in \{0.1, 0.25, 0.5, 1.0\}$  on the checkerboard. To ensure proper comparison, the UV and IR cutoffs are defined such that the coordinate  $z \equiv (pr)^{1/p}$  in the propagator (A6) satisfies  $z_{\text{IR}} = 1$  and  $z_{\text{UV}} = 1/e$ , analogous to the choice made in the GenAdS models (where  $z = e^{-r}$ ). The results are in Figure 5.

These models are not as good as the analogous GenAdS model shown in Figure 4 ( $\Delta = 2.0$ ) both in terms of BV and WED. That said, there is room for hyperparameter optimization. For example, adjusting the cutoff values can improve model performance.

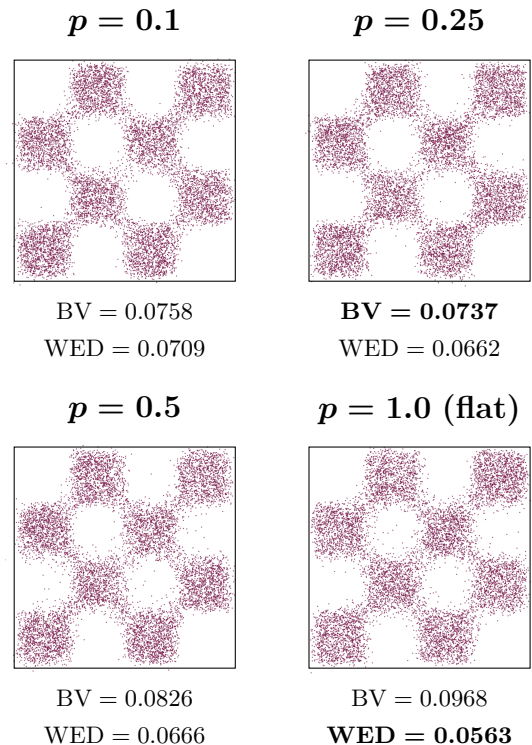


FIG. 5: The results from dialing the HSV parameter  $p$ . These models have  $m^2 = 0$  and are trained to 100 epochs.

	100 epochs	250 epochs	500 epochs	1,500 epochs
<b>AdS + KG (H)</b>				
<b>AdS + KG (L)</b>				
<b>AdS</b>				
<b>Baseline CNN</b>				

FIG. 6: The ablation experiment for MNIST. We present samples generated by four different models—**AdS + KG (H)**, **AdS + KG (L)**, **AdS**, and **Baseline CNN**—after 100, 250, 500, and 1500 training epochs. The first three are models using AdS physics, with **AdS + KG (H)** trained on the residual loss (49) with a Hermite path (45), **AdS + KG (L)** trained on the residual loss with a linear path (44), and **AdS** trained to learn the full velocity with the loss (46) with a linear path. The **Baseline CNN** is free of AdS physics but is still trained using flow matching with a linear path.

## VI. GENERATING MNIST

The Modified National Institute of Standards and Technology (MNIST) dataset of hand-drawn numbers is standard in tests of computer vision [27]. While MNIST is simple for an image dataset, its dimensionality is much higher than the checkerboard; each image has  $28^2 = 784$  pixels. Generating MNIST is thus a good test of whether GenAdS viably scales to higher dimensional data.

We still use  $\text{AdS}_3$  ( $d = 2$ ) with  $\Delta = 1.5$ . This time,

however, samples are not encoded via  $\delta$  sources on the boundary; we instead use the pixel intensity maps as sources. The velocity CNN has 13,448,514 parameters for the Hermite path and 13,449,668 parameters for the linear path—higher capacity than those in Section V. We train on 10,000 samples per epoch with batch size 128, using AdamW with learning rate  $3 \times 10^{-4}$  and weight decay  $1 \times 10^{-5}$ . The parameters for the base distribution are (60). Lastly, for the spectral parameters we take  $L = K = 28$ , so there are 784 Fourier modes.

### VI.1. MNIST metric

For evaluation of the final models, we report the Fréchet inception distance (FID) [28]. This metric is often used to assess image quality in larger image datasets such as CIFAR-10. In summary, it computes the difference between ground-truth and model distributions in a feature space learned by a pretrained Inception network [29], so FID quantifies high-level semantic differences.

Specifically, for a set of images, we model the feature-space distributions as multivariate Gaussians. Taking a set of  $N$  images  $\{X_i\}$ , we denote the learned feature vector of the Inception network as a multivariate function  $\vec{\mathcal{F}}(X_i)$ . The mean  $\vec{\mu}$  and covariance  $\Sigma$  are

$$\vec{\mu} \equiv \frac{1}{N} \sum_{i=1}^N \vec{\mathcal{F}}(X_i), \quad (65)$$

$$\Sigma \equiv \frac{1}{N-1} \sum_{i=1}^N \left[ \vec{\mathcal{F}}(X_i) - \vec{\mu} \right] \left[ \vec{\mathcal{F}}(X_i) - \vec{\mu} \right]^T \quad (66)$$

The FID is then defined as the 2-Wasserstein distributional distance between the Gaussians  $\mathcal{N}(\vec{\mu}_r, \Sigma_r)$  and  $\mathcal{N}(\vec{\mu}_g, \Sigma_g)$  respectively corresponding to real and generated data. This distance has the following closed form:

$$\text{FID} = |\vec{\mu}_r - \vec{\mu}_g| + \text{Tr} \left[ \Sigma_r + \Sigma_g - 2(\Sigma_r \Sigma_g)^{1/2} \right]. \quad (67)$$

If the two distributions are the same, then  $\text{FID} = 0$ . As such, lower FID indicates better agreement between the generated samples and the ground-truth distribution.

### VI.2. Ablations with MNIST

As in Section V.2, we conduct an ablation study for the model trained on MNIST. We use the same GenAdS models as before—one trained with the residual loss (49) with a Hermite path (45), another trained with the residual loss with a linear path (44), and a third trained with the full loss (46) with a linear path. However, this time we use a CNN as our baseline model, since CNNs are better at generating images than FCNs due to the former’s inductive bias towards translational equivariance. The baseline has the same exact architecture as the linear GenAdS CNNs, with 13,449,668 parameters. Furthermore, there are no significant differences in the training times across models, so here we simply consider the number of epochs as a suitable proxy.

We show generated samples taken from each model after 100, 250, 500, and 1,500 epochs in Figure 6. These indicate that the fully physics-informed model using the residual loss (49) and the Hermite path (45) is actually *worse* than the others, whereas the ablated GenAdS models are comparable to the baseline. This is also evident from the final BPM and FID values (Table I).

Models	FID ( $\pm$ std)
AdS + KG (H)	$38.170 \pm 0.449$
AdS + KG (L)	<b><math>21.762 \pm 2.021</math></b>
AdS	$22.703 \pm 1.659$
Baseline CNN	$21.991 \pm 2.897$

TABLE I: Fréchet inception distance (FID)  $\pm$  standard deviations, averaged over three seeds, for each of the models trained on MNIST for 1500 epochs.

## VII. CONCLUSIONS AND OUTLOOK

The GenAdS framework represents an initial step toward leveraging the rich mathematical structure of gauge/gravity duality for generative modeling. While the current implementation employs significant simplifications, our experiments reveal several first-pass results that illustrate the utility of GenAdS and areas for future development.

We speculate that use of information from AdS physics provides inductive bias in guiding early training. In the checkerboard, this leads to an increase in training efficiency, which is in line with the results typically seen in physics-informed neural networks [6]. However, unlike in those models, we conclude that the key facet of GenAdS is the holographic encoding and inclusion of AdS geometry, rather than any dynamical input such as the inclusion of physical equations of motion. Indeed, the threshold times shown in Figure 3 indicate that the **AdS** model using a linear path and a full (rather than residual) velocity network is the fastest converging model for the checkerboard. Furthermore as indicated by the MNIST experiment, injecting too much physics might also damage performance, whereas the **AdS** model is our most flexible.

That said, our implementation of holographic encoding is simple, particularly for images. Perhaps more carefully tailored approaches could further enhance model performance. For example, one could represent individual pixels as a collection of spatially arranged point sources. This would be a natural extension of the point encoding used for the checkerboard to higher-dimensional datasets. However, this would also require more refined decoding algorithms than what we have implemented here.

We have also connected model performance to the underlying physics through some of our experiments. In the tests where we vary  $\Delta$ , we cover three qualitatively different cases:  $1 < \Delta < 2$ ,  $\Delta = 2$ , and  $\Delta > 2$ . For  $d = 2$ , these respectively correspond to negative, zero, and positive values of  $m^2$ . The boundary interpretation is that the boundary scalar triggers a relevant, marginal, or irrelevant deformation, respectively [21]. So intuitively, the model is more unstable for  $\Delta > 2$ , i.e. scalars that are irrelevant in the IR (i.e. deep in the bulk).

The experiments with the hyperscaling-violating geometries illustrate that our framework does not inherently require AdS. However, these experiments also

demonstrate the flexibility of AdS, in that the HSV implementation cannot be easily extended beyond the massless case due to a lack of closed-form expressions. In fact, if we were to consider massive scalars, stability conditions would mandate that we use  $m^2 > 0$ . Hypothetically, if the finding of the previous experiment—that higher  $m^2$  leads to worse models—also holds in HSV geometries, then we might expect AdS with  $m^2 < 0$  to maintain an edge in performance anyway.

Future work will focus on non-Euclidean data. We have only considered planar datasets, but AdS can be written in other slicings. For example, a version of GenAdS using a spherical slicing of AdS might be a natural arena with which to generate datasets on the sphere.

There are also other ways in which we can use the structure of AdS for generation. Instead of considering physical theories, one might make use of geometric structure. Indeed, AdS geometry has long been known in the AdS/CFT community to encode universal information about the boundary—see for example the relationship between CFT entanglement entropy and minimal-area surfaces first elucidated by Ryu and Takayanagi [30].

Lastly, a more ambitious goal is to incorporate fuller gravitational dynamics into our GenAdS model. Put another way, one might hope to construct a model that also accounts for backreaction of the metric in response to the scalar dynamics. The resulting flow equations are significantly more complicated than just Klein–Gordon itself, since they would involve first and second derivatives of the metric tensor. However, such systems also have clear interpretations in the language of renormalization group (RG) flow, which has been linked to optimal transport and diffusion [31, 32]. As such, GenAdS with backreaction could serve as a geometric manifestation of this connection between generative modeling and RG flow.

AdS/CFT and holography provide the foundation for a novel type of generative model with significant potential for theoretical and practical extension in the future. Our results with this first pass of GenAdS demonstrate that rather abstract concepts from quantum gravity and holography can inform novel machine learning architectures that leverage physics and yield concrete advances in the development of generative modeling.

## VIII. ACKNOWLEDGMENTS

SS and ES were supported by the U.S. Department of Energy (DOE) grant DE-SC001010. EM, SS, and RM were supported by the National Science Foundation STTR award 2451680. DV was supported by DOE grant DE-SC0024563. RM was also supported by NSF Access Maximize allocation number BIO220163 and the DOE National Energy Research Scientific Computing Center (NERSC).

## Appendix A: Hyperscaling-violating geometries

In Section V.4, we apply our holographic flow-matching machinery to hyperscaling-violating (HSV) geometries [26]. Here, we discuss the theoretical details and formulas used in our implementation.

The HSV metric is most naturally described by the following form:

$$ds^2 = \frac{1}{z^{2(1-p)}} (dz^2 + d\vec{x}^2), \quad z > 0, \quad p \in (0, 1]. \quad (\text{A1})$$

This metric has a boundary at  $z = 0$ . In the AdS case  $p \rightarrow 0$ , this is the location of the dual CFT, while in flat space  $p \rightarrow 1$  (and only in flat space) this boundary is an artificial cutoff. For the interpolating geometries, the boundary is the slice on which the metric diverges.

In this Appendix, we recast this in terms of the warped ansatz (1), leading to the metric (64) in the main text, and present the formulas needed for our HSV experiment.

### 1. Rewriting the metric

For  $p \in (0, 1]$ , we can transform the radial coordinate  $z$ , which is strictly positive, by defining  $r \equiv z^p/p$ . This power-law transformation yields the warped metric (1):

$$ds^2 = dr^2 + \frac{1}{(pr)^{2\gamma}} d\vec{x}^2, \quad \gamma \equiv \frac{1}{p} - 1 \in [0, \infty). \quad (\text{A2})$$

This is qualitatively different from the metric for AdS, in that the function multiplying the radial slices is a power rather than an exponential. In fact, in the limit  $p \rightarrow 0$  for which (A1) reduces to AdS, the  $r$ -dependent metric develops a coordinate singularity. Furthermore, the radial coordinate  $r$  runs over the interval  $(0, \infty)$ , with  $r = 0$  being the boundary rather than  $r = \infty$ , so the cutoffs  $r_{\text{IR}}$  and  $r_{\text{UV}}$  must satisfy  $r_{\text{UV}} < r_{\text{IR}}$ .

As in planar AdS, we write the scalar field as a linear combination of cubic Hermite polynomials parameterized by  $u \in [0, 1]$ , which is related to  $r$  by (39). However, the explicit formula for  $u(r)$  is different for HSV geometries:

$$u(r) = \frac{r_{\text{IR}}^{d\gamma+1} - r^{d\gamma+1}}{r_{\text{IR}}^{d\gamma+1} - r_{\text{UV}}^{d\gamma+1}}. \quad (\text{A3})$$

### 2. Solving Klein–Gordon

Let us now construct the propagator. Recall that the scalar field  $\Phi$  has the following Fourier decomposition:

$$\Phi(r, \vec{x}) = \int \frac{d^d x}{(2\pi)^{d/2}} e^{-i\vec{k} \cdot \vec{x}} \phi_{\vec{k}}(r). \quad (\text{A4})$$

The Fourier-space equation for the mode coefficient  $\phi_{\vec{k}}$  with momentum  $\vec{k}$  can be written by identifying  $\lambda = |\vec{k}|^2$  and  $f(r) = (pr)^{-\gamma}$  in (14), which yields

$$\frac{d^2 \phi_{\vec{k}}}{dr^2} - \frac{d\gamma}{r} \frac{d\phi_{\vec{k}}}{dr} = \left[ (pr)^{2\gamma} |\vec{k}|^2 + m^2 \right] \phi_{\vec{k}}(r). \quad (\text{A5})$$

This is also the differential equation for the associated propagator in momentum space. However, unlike in AdS, the massive equation cannot be solved in closed form [26].

In contrast, for a massless scalar ( $m^2 = 0$ ), this equation admits a closed-form solution. Assuming regularity and normalizing to 1 as  $r \rightarrow 0$ , we find that

$$\kappa_{|\vec{k}|}(r) = \frac{\left[(pr)^{1/p}|\vec{k}|\right]^\beta}{2^{\beta-1}\Gamma(\beta)} K_\beta \left((pr)^{1/p}|\vec{k}|\right), \quad (\text{A6})$$

$$\beta = \frac{1 + (d-1)(1-p)}{2}.$$

Furthermore, by setting  $m^2 = 0$  and taking the terms dominant as  $r \rightarrow 0$  in (A5), we find that  $\phi_{\vec{k}}$  exhibits the following asymptotic behavior:

$$\phi_{\vec{k}} \sim J(\vec{k}) + r^{d\gamma+1} \phi_1(\vec{k}), \quad (\text{A7})$$

where  $J$  is the source while  $\phi_1$  is analogous to the VEV in (5). Since the source is already  $O(1)$  whereas the “VEV” decays when  $r \rightarrow 0$ , there is no need to perform a field redefinition for numerical stability.

So, we perform flow matching with the fields  $\Phi$  and  $\Pi \equiv \partial_r \Phi$ . In Fourier space, the first-order massless Klein–Gordon equations are

$$\frac{d\phi_{\vec{k}}}{dr} = \pi_{\vec{k}}(r), \quad (\text{A8})$$

$$\frac{d\pi_{\vec{k}}}{dr} = (pr)^{2\gamma} |\vec{k}|^2 \phi_{\vec{k}}(r) + \frac{d\gamma}{r} \pi_{\vec{k}}(r). \quad (\text{A9})$$

Equipped with all of these formulas, the approach is the same as in AdS. We still use spectral point encoding and compute residual losses in Fourier space to train the model, as discussed in Section IV, but with the propagator, mode equations, and Hermite-path parameter adapted to the HSV geometries.

---

[1] J. Sohl-Dickstein, E. Weiss, N. Maheswaranathan, and S. Ganguli, in *International Conference on Machine Learning*, Vol. 37 (2015) pp. 2256–2265, [arXiv:1503.03585 \[cs.LG\]](#).

[2] J. Ho, A. Jain, and P. Abbeel, in *Neural Information Processing Systems*, Vol. 33 (2020) [arXiv:2006.11239 \[cs.LG\]](#).

[3] R. T. Q. Chen, Y. Rubanova, J. Bettencourt, and D. Duvenaud, in *Neural Information Processing Systems*, Vol. 31 (2018) [arXiv:1806.07366 \[cs.LG\]](#).

[4] W. Grathwohl, R. T. Q. Chen, J. Bettencourt, I. Sutskever, and D. Duvenaud, in *International Conference on Learning Representations* (2019) [arXiv:1810.01367 \[cs.LG\]](#).

[5] Y. Lipman, R. T. Q. Chen, H. Ben-Hamu, M. Nickel, and M. Le, in *International Conference on Learning Representations* (2023) [arXiv:2210.02747 \[cs.LG\]](#).

[6] M. Raissi, P. Perdikaris, and G. Karniadakis, *Journal of Computational Physics* **378**, 686–707 (2019).

[7] F. Djeumou, C. Neary, E. Goubault, S. Putot, and U. Topcu, in *Learning for Dynamics and Control*, Vol. 168 (2022) pp. 263–277, [arXiv:2109.06407 \[cs.LG\]](#).

[8] Z. Liu, D. Luo, Y. Xu, T. Jaakkola, and M. Tegmark, arXiv e-prints (2023), [arXiv:2304.02637 \[cs.LG\]](#).

[9] R. T. Q. Chen and Y. Lipman, in *International Conference on Learning Representations* (2024) [arXiv:2302.03660 \[cs.LG\]](#).

[10] G. 't Hooft, in *Salamfestschrift* (1993) [arXiv:gr-qc/9310026 \[gr-qc\]](#).

[11] L. Susskind, *J. Math. Phys.* **36**, 6377 (1995), [arXiv:hep-th/9409089 \[hep-th\]](#).

[12] J. M. Maldacena, *Adv. Theor. Math. Phys.* **2**, 231 (1998), [arXiv:hep-th/9711200 \[hep-th\]](#).

[13] E. Witten, *Adv. Theor. Math. Phys.* **2**, 253 (1998), [arXiv:hep-th/9802150](#).

[14] V. Balasubramanian and P. Kraus, *Phys. Rev. Lett.* **83**, 3605 (1999), [arXiv:hep-th/9903190 \[hep-th\]](#).

[15] J. de Boer, E. P. Verlinde, and H. L. Verlinde, *JHEP* **08**, 003, [arXiv:hep-th/9912012 \[hep-th\]](#).

[16] B. Swingle, *Phys. Rev. D* **86**, 065007 (2012), [arXiv:0905.1317 \[cond-mat.str-el\]](#).

[17] M. Van Raamsdonk, *Gen. Rel. Grav.* **42**, 2323 (2010), [arXiv:1005.3035 \[hep-th\]](#).

[18] F. Pastawski, B. Yoshida, D. Harlow, and J. Preskill, *JHEP* **06**, 149, [arXiv:1503.06237 \[hep-th\]](#).

[19] K. Hashimoto, S. Sugishita, A. Tanaka, and A. Tomiya, *Phys. Rev. D* **98**, 046019 (2018), [arXiv:1802.08313 \[hep-th\]](#).

[20] M. Zhdanov, N. Iqbal, E. Bekkers, and P. Forré, in *ICLR Workshop on Machine Learning Multiscale Processes* (2025) [arXiv:2505.12880 \[cs.LG\]](#).

[21] O. Aharony, S. S. Gubser, J. M. Maldacena, H. Ooguri, and Y. Oz, *Phys. Rept.* **323**, 183 (2000), [arXiv:hep-th/9905111](#).

[22] I. R. Klebanov and E. Witten, *Nucl. Phys. B* **556**, 89 (1999), [arXiv:hep-th/9905104 \[hep-th\]](#).

[23] P. Breitenlohner and D. Z. Freedman, *Phys. Lett. B* **115**, 197 (1982).

[24] T. Banks, M. R. Douglas, G. T. Horowitz, and E. J. Martinec, arXiv e-prints (1998), [arXiv:hep-th/9808016 \[hep-th\]](#).

[25] D. Harlow and D. Stanford, arXiv e-prints (2011), [arXiv:1104.2621 \[hep-th\]](#).

[26] L. Huijse, S. Sachdev, and B. Swingle, *Phys. Rev. B* **85**, 035121 (2012), [arXiv:1112.0573 \[cond-mat.str-el\]](#).

[27] Y. LeCun, L. Bottou, Y. Bengio, and P. Haffner, *Proceedings of the IEEE* **86**, 2278 (1998).

[28] M. Heusel, H. Ramsauer, T. Unterthiner, B. Nessler, and S. Hochreiter, in *Neural Information Processing Systems*, Vol. 30 (2017) [arXiv:1706.08500 \[cs.LG\]](#).

[29] C. Szegedy, V. Vanhoucke, S. Ioffe, J. Shlens, and Z. Wojna, in *IEEE Conference on Computer Vision and Pattern Recognition* (2016) [arXiv:1512.00567 \[cs.CV\]](#).

[30] S. Ryu and T. Takayanagi, *Phys. Rev. Lett.* **96**, 181602 (2006), [arXiv:hep-th/0603001](#).

[31] J. Cotler and S. Reznikov, *Phys. Rev. D* **108**, 025003 (2023), [arXiv:2202.11737 \[hep-th\]](#).

[32] J. Cotler and S. Reznikov, arXiv e-prints (2023), [arXiv:2308.12355 \[hep-th\]](#).